

**Structural properties of Bi<sub>2</sub>Te<sub>3</sub> topological insulator thin films grown by molecular beam epitaxy on (111) BaF<sub>2</sub> substrates**

Celso I. Fornari, Paulo H. O. Rappl, Sérgio L. Morelhão, and Eduardo Abramof

Citation: *Journal of Applied Physics* **119**, 165303 (2016); doi: 10.1063/1.4947266

View online: <http://dx.doi.org/10.1063/1.4947266>

View Table of Contents: <http://scitation.aip.org/content/aip/journal/jap/119/16?ver=pdfcov>

Published by the **AIP Publishing**

---

**Articles you may be interested in**

[Magnetotransport study of \(Sb<sub>1-x</sub>Bi<sub>x</sub>\)<sub>2</sub>Te<sub>3</sub> thin films on mica substrate for ideal topological insulator](#)  
*AIP Advances* **6**, 055812 (2016); 10.1063/1.4943156

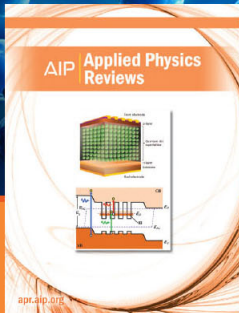
[Growth and characterization of molecular beam epitaxy-grown Bi<sub>2</sub>Te<sub>3</sub>-xSex topological insulator alloys](#)  
*J. Appl. Phys.* **119**, 055303 (2016); 10.1063/1.4941018

[High-quality Bi<sub>2</sub>Te<sub>3</sub> thin films grown on mica substrates for potential optoelectronic applications](#)  
*Appl. Phys. Lett.* **103**, 031605 (2013); 10.1063/1.4813903

[Molecular beam epitaxy of bilayer Bi\(111\) films on topological insulator Bi<sub>2</sub>Te<sub>3</sub>: A scanning tunneling microscopy study](#)  
*Appl. Phys. Lett.* **101**, 081603 (2012); 10.1063/1.4747715

[Epitaxial growth of Bi<sub>2</sub>Se<sub>3</sub> topological insulator thin films on Si \(111\)](#)  
*J. Appl. Phys.* **109**, 103702 (2011); 10.1063/1.3585673

---



**NEW Special Topic Sections**

**NOW ONLINE**  
Lithium Niobate Properties and Applications:  
Reviews of Emerging Trends

**AIP** | Applied Physics Reviews

## Structural properties of Bi<sub>2</sub>Te<sub>3</sub> topological insulator thin films grown by molecular beam epitaxy on (111) BaF<sub>2</sub> substrates

Celso I. Fornari,<sup>1,a)</sup> Paulo H. O. Rappi,<sup>1</sup> Sérgio L. Morelhão,<sup>2</sup> and Eduardo Abramof<sup>1</sup>

<sup>1</sup>LAS, Instituto Nacional de Pesquisas Espaciais, CP 515, 12245-970 São José dos Campos, SP, Brazil

<sup>2</sup>Instituto de Física, Universidade de São Paulo, CP 66318, 05315-970 São Paulo, SP, Brazil

(Received 10 February 2016; accepted 9 April 2016; published online 26 April 2016)

Structural properties of topological insulator bismuth telluride films grown epitaxially on (111) BaF<sub>2</sub> with a fixed Bi<sub>2</sub>Te<sub>3</sub> beam flux were systematically investigated as a function of substrate temperature and additional Te flux. A layer-by-layer growth mode is observed since the early stages of epitaxy and remains throughout the whole deposition. Composition of the epitaxial films produced here stays between Bi<sub>2</sub>Te<sub>3</sub> and Bi<sub>4</sub>Te<sub>5</sub>, as determined from the comparison of the measured x-ray diffraction curves with calculations. The substrate temperature region, where the growth rate remains constant, is found to be the most appropriate to obtain ordered Bi<sub>2</sub>Te<sub>3</sub> films. Line width of the  $L = 18$  Bi<sub>2</sub>Te<sub>3</sub> diffraction peaks as low as 140 arcsec was obtained, indicating high crystalline quality. Twinning domains density rises with increasing growth temperature and reducing Te extra flux. X-ray reflectivity curves of pure Bi<sub>2</sub>Te<sub>3</sub> films with thickness from 165 to 8 nm exhibited well defined interference fringes, evidencing homogeneous layers with smooth surface. Our results demonstrate that Bi<sub>2</sub>Te<sub>3</sub> films with very well controlled structural parameters can be obtained. High structural quality Bi<sub>2</sub>Te<sub>3</sub> films as thin as only eight quintuple layers grown here are promising candidates for intrinsic topological insulator. *Published by AIP Publishing.*

[<http://dx.doi.org/10.1063/1.4947266>]

### INTRODUCTION

Bismuth telluride has long been known to have a high room-temperature figure of merit (ZT) among the thermoelectric materials.<sup>1–3</sup> Recently, it has attracted intense interest due to its pronounced features as a member of a new class of materials called three-dimensional topological insulators, which are insulating in the bulk and exhibit gapless metallic surface states with linear energy-momentum dispersion shaped like a Dirac cone. Due to the strong spin-orbit coupling, these conducting surface states have electron momentum locked to the spin orientation and are protected from scattering mechanisms by time reversal symmetry. Consequently, high-mobility spin polarized surface currents can be produced without external magnetic fields, offering possibilities to new applications in spintronics or quantum computing.<sup>4–6</sup>

The topological order in V-VI compounds has been theoretically predicted<sup>7–9</sup> and the existence of the metallic surface states has been confirmed by angle resolved photoelectron spectroscopy (ARPES) experiments in bulk single crystals of Bi<sub>1–x</sub>Sb<sub>x</sub>,<sup>10</sup> Bi<sub>2</sub>Se<sub>3</sub>,<sup>11,12</sup> Sb<sub>2</sub>Te<sub>3</sub>, and Bi<sub>2</sub>Te<sub>3</sub>.<sup>13,14</sup> ARPES has demonstrated to be a powerful technique to characterize the conducting surface states, providing the experimental signature of a three-dimensional topological insulator. The bulk samples are cleaved inside the vacuum chamber in order to obtain a fresh surface for ARPES and, even in ultra high vacuum (UHV) conditions, aging effects have been reported.<sup>15,16</sup> The oxide layer formed by air exposure on the V-VI crystal surface degrades the metallic states.

In case of Bi<sub>2</sub>Te<sub>3</sub>, an oxide layer of 1 nm is formed after around 1 day at room conditions.<sup>16,17</sup> The contribution of the Dirac surface states to electrical conductivity measurements is hindered by bulk conduction due to free carriers produced by crystalline defects like vacancies and anti-sites in the V-VI alloys. Besides surface oxidation, this bulk conduction hampers electrical measurements of the metallic surface states in three-dimensional topological insulators. Counter doping, like Ca for Bi<sub>2</sub>Se<sub>3</sub><sup>11</sup> and Sn for Bi<sub>2</sub>Te<sub>3</sub>,<sup>14</sup> has been used to move the Fermi level inside the band gap to obtain insulating bulk samples. However, high doping affects carrier transport and conduction only through topological surface states has shown instabilities in time scale of hours during ARPES experiments.<sup>18</sup> In order to obtain intrinsic topological insulators, molecular beam epitaxy (MBE) has been applied to grow bismuth chalcogenide layers. Due to the control at the atomic level and reproducibility of the MBE technique, high structural quality bismuth chalcogenide films are obtained, where the bulk conduction is expected to be suppressed.

Epitaxial films of bismuth telluride have been grown by MBE on different types of substrates like (111) Si, (111) GaAs, and (0001) Al<sub>2</sub>O<sub>3</sub>.<sup>19–22</sup> In case of the Bi<sub>2</sub>Te<sub>3</sub> epitaxy on (111) Si, a small lattice mismatch near to 1% is found if a supercell of both materials is considered, which enables the growth of high crystalline quality films.<sup>19</sup> Despite the large lattice mismatch to Bi<sub>2</sub>Te<sub>3</sub> of 8.7% for both GaAs and Al<sub>2</sub>O<sub>3</sub>, epitaxial layers with relatively good structural quality have been achieved on these substrates as van der Waals bonds inside Bi<sub>2</sub>Te<sub>3</sub> crystal structure accommodate the in-plane differences in lattice parameters.<sup>22</sup> Due to the small lattice mismatch of only 0.04% to Bi<sub>2</sub>Te<sub>3</sub>, (111) BaF<sub>2</sub> has

<sup>a)</sup>Author to whom correspondence should be addressed. Electronic mail: celso.fornari@inpe.br. Tel.: +55 12 3208-6681.

been shown to be an appropriate substrate to grow bismuth telluride.<sup>23–25</sup> The films can be grown by MBE using either separated Bi and Te solid sources<sup>19–23</sup> or a  $\text{Bi}_2\text{Te}_3$  compound effusion source and additional Te cell.<sup>24,25</sup> Depending on the growth parameters, other phases of  $\text{Bi}_x\text{Te}_y$  compounds can be obtained and the conditions to achieve single phase  $\text{Bi}_2\text{Te}_3$  are located in a narrow window. Most recently, intrinsic conduction through topological surface states has been reported for very thin (10–50 nm) insulating  $\text{Bi}_2\text{Te}_3$  epitaxial films, as demonstrated by ARPES and four-point probe conductivity measurements performed at room temperature in the same UHV system. However, conduction through Dirac surface states vanishes after air exposure in time scale of minutes, indicating that a capping layer is essential to protect topological state and explore these new features in room conditions.<sup>26</sup> Determination of optimum growth parameters to obtain high-quality  $\text{Bi}_2\text{Te}_3$  epitaxial layers with well controlled structural properties is therefore crucial for practical applications.

Contrary to conventional zinc-blend and rock-salt semiconductor compounds, bismuth telluride can exist in different  $\text{Bi}_x\text{Te}_y$  phases, depending on the growth conditions. The  $\text{Bi}_x\text{Te}_y$  compounds constitute a homologous series of crystal structures derived from an ordered stacking of  $\text{Te}^1\text{-Bi-Te}^2\text{-Bi-Te}^1$  quintuple layers (QLs) and Bi-Bi bilayers (BLs) building blocks, forming the  $(\text{Bi}_2)_M(\text{Bi}_2\text{Te}_3)_N$  adaptative series<sup>27</sup> shown in Figure 1. This series spans from the Te-richest phase  $\text{Bi}_2\text{Te}_3$  (M:N=0:3) to pure bismuth (M:N=3:0), passing through a series of phases such as  $\text{Bi}_4\text{Te}_5$  (M:N=1:5),  $\text{Bi}_6\text{Te}_7$  (M:N=2:7),  $\text{Bi}_8\text{Te}_9$  (M:N=3:9),  $\text{BiTe}$  (M:N=1:2), and  $\text{Bi}_4\text{Te}_3$  (M:N=3:3). The entire series can be written in terms of the Te deficit  $\delta$  as  $\text{Bi}_2\text{Te}_{3-\delta}$ , where  $\delta = 3M/(M+N)$ . Except in the limiting

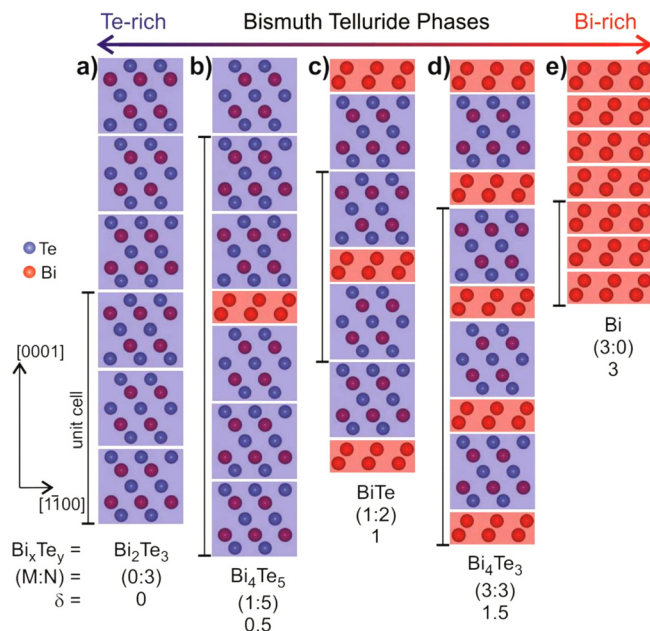


FIG. 1. Crystal structure representation of  $\text{Bi}_x\text{Te}_y$  compounds in the ordered homologous  $(\text{Bi}_2)_M(\text{Bi}_2\text{Te}_3)_N$  series: (a)  $\text{Bi}_2\text{Te}_3$ , (b)  $\text{Bi}_4\text{Te}_5$ , (c)  $\text{BiTe}$ , (d)  $\text{Bi}_4\text{Te}_3$ , and (e) Bi. Building blocks of  $\text{Bi}_2\text{Te}_3$  quintuple layers and Bi bilayers are shown in violet and red, respectively. The entire series can be expressed as  $\text{Bi}_2\text{Te}_{3-\delta}$ , where  $\delta = 3M/(M+N)$  is the Te deficit. The lattice periodicity of each compound is indicated aside.<sup>27</sup>

cases,  $\delta = 0$  and  $\delta = 3$ , the addition of Bi-Bi bilayers in between the quintuple layers during molecular beam epitaxial growth does not occur uniformly, but as a statistical distribution where the grown films can be considered as a random one-dimensional  $\text{Bi}_x\text{Te}_y$  alloy rather than as an ordered homologous  $(\text{Bi}_2)_M(\text{Bi}_2\text{Te}_3)_N$  structure.<sup>25</sup>

Like other V-VI compounds,  $\text{Bi}_2\text{Te}_3$  crystallizes in a tetradymite-type structure shown in Figure 2(a). The unit cell of this hexagonal lattice is described by stacking of three  $\text{Te}^1\text{-Bi-Te}^2\text{-Bi-Te}^1$  quintuple layers along  $c$ -direction. Inside the QL, the neighboring Bi-Te atoms are ionic bonded and the adjacent QLs are van der Waals coupled to each other by the facing  $\text{Te}^1\text{-Te}^1$  layers. This van der Waals gap gives the structure an anisotropic character similar to other layered materials. The lattice parameter along  $[0001]$  direction of the  $\text{Bi}_2\text{Te}_3$  bulk material is  $c = 30.474 \text{ \AA}$ . Figure 2(b) shows the  $(0001)$   $\text{Bi}_2\text{Te}_3$  surface with the three topmost atomic layers, which form a hexagonal lattice with an in-plane lattice parameter  $a = 4.382 \text{ \AA}$ . The atomic rows along the symmetry azimuths  $[11\bar{2}0]$  and  $[10\bar{1}0]$ , rotated by  $30^\circ$  to each other, are separated by  $a/2\sqrt{3}$  and  $a/2$ , respectively. As the in-plane lattice constant of the  $(111)$   $\text{BaF}_2$  surface  $a_{\parallel}^{\text{BaF}_2} = a_0^{\text{BaF}_2} / \sqrt{2} = 4.384 \text{ \AA}$  is almost equal to the hexagonal lattice constant of  $\text{Bi}_2\text{Te}_3$ , the small lattice mismatch of only 0.04% between both materials makes  $(111)$   $\text{BaF}_2$  a suitable substrate for the epitaxy of bismuth telluride. In this epitaxy, the  $(0001)$   $\text{Bi}_2\text{Te}_3$  hexagonal planes are parallel to the  $(111)$  cubic  $\text{BaF}_2$  planes and the  $[\bar{1}10]$  azimuth of the substrate cubic lattice is parallel to the  $[11\bar{2}0]$  azimuth of the film hexagonal lattice.

This work presents a systematic investigation of the structural properties of bismuth telluride thin films grown by molecular beam epitaxy on  $(111)$   $\text{BaF}_2$  substrates, using a nominal stoichiometric  $\text{Bi}_2\text{Te}_3$  solid source and additional

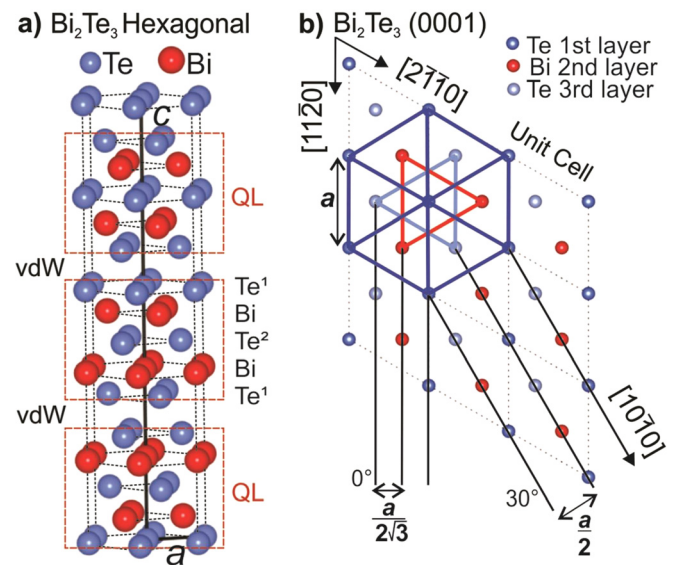


FIG. 2. (a) Hexagonal crystalline structure of  $\text{Bi}_2\text{Te}_3$ . The unit cell is formed by stacking of three  $\text{Te}^1\text{-Bi-Te}^2\text{-Bi-Te}^1$  quintuple layers (QL) along  $[0001]$  direction. The van der Waals (vdW) coupling between adjacent QLs through  $\text{Te}^1$  atoms is much weaker than that between Te-Bi inside the QL. (b)  $(0001)$   $\text{Bi}_2\text{Te}_3$  surface showing the three uppermost atomic layers, evidencing the hexagonal unit cell with lattice parameter  $a$  and the three symmetry azimuths.

Te cells. The growth conditions were varied in a wide range of substrate temperature and Te/Bi<sub>2</sub>Te<sub>3</sub> beam flux ratio. The epitaxial films were characterized *in situ* by reflection high-energy electron diffraction (RHEED) and *ex situ* by high-resolution x-ray diffraction, x-ray reflectometry, and field-emission gun microscopy.

## EXPERIMENTAL

Bismuth telluride epitaxial films were grown on freshly cleaved (111) BaF<sub>2</sub> substrates, from Korth Kristalle GmbH, in a Riber 32P molecular beam epitaxial system using an effusion cell charged with nominal stoichiometric Bi<sub>2</sub>Te<sub>3</sub> solid source and two additional Te cells to offer the extra Te flux. The Bi<sub>2</sub>Te<sub>3</sub> charge was synthesized in our laboratory from commercially available Bi (99.999%) and Te (99.9999%) elemental materials. For all growths, four thin substrate slices were fixed with an eutectic indium-gallium solution to the molybdenum substrate holder. The beam fluxes were monitored by a Bayer-Alpert ion gauge moved to the substrate position before and after each growth. The beam equivalent pressure (BEP) of the Bi<sub>2</sub>Te<sub>3</sub> and Te fluxes was measured and the flux ratio  $\Phi_R = \text{BEP}^{\text{Te}}/\text{BEP}^{\text{Bi}_2\text{Te}_3}$  was determined. The BaF<sub>2</sub> substrates were pre-heated at 300 °C for 10 min before starting the growth. The background pressure of the growth chamber was maintained at 10<sup>-9</sup> Torr during growth.

To monitor *in situ* the film surface during growth, reflection high-energy electron diffraction (RHEED) patterns were acquired using a 35 keV RHEED system equipped with a CCD camera in front of the fluorescent screen and a data acquisition setup. The kSA 400 software package was used to analyze the recorded RHEED movies.

X-ray diffraction measurements were performed in a PANalytical X'Pert MRD high-resolution x-ray diffractometer equipped with (220) Ge four-crystal monochromator adjusted for Cu K $\alpha_1$  radiation and an open detector with acceptance of 1°. For the twinning characterization, the same configuration of the x-ray diffractometer is used to perform azimuthal scans for a fixed Bi<sub>2</sub>Te<sub>3</sub> asymmetric Bragg peak.

To measure the grazing incidence x-ray reflectivity of Bi<sub>2</sub>Te<sub>3</sub>/BaF<sub>2</sub> films, the high-resolution x-ray diffractometer configuration is changed. In this configuration, the Cu x-ray tube is set to line focus and the incident beam optics is composed of a Soller slit with an axial divergence of 2.5°, a 1/32° divergence slit, a Ni filter, and an attenuator, and for the reflected beam of a parallel beam collimator, a 0.1 mm anti-scatter slit and a flat-crystal graphite monochromator.

Cross section images of Bi<sub>2</sub>Te<sub>3</sub>/BaF<sub>2</sub> films were acquired using a TESCAN MIRA3 field-emission gun microscopy equipped with an energy dispersive x-ray detector.

## RESULTS AND DISCUSSION

### Molecular beam epitaxy

For this work, a series of samples was produced with the beam equivalent pressure of the Bi<sub>2</sub>Te<sub>3</sub> cell kept constant at  $5 \times 10^{-7}$  Torr and varying the substrate temperature between 180 °C and 310 °C and the Te/Bi<sub>2</sub>Te<sub>3</sub> flux ratio  $\Phi_R$  from 0 to

2. The thickness of the films was measured by interference fringes in x-ray reflectivity curves and/or by field-emission gun microscopy cross section images. The growth time for all samples was 2 h, except for the series produced to x-ray reflectivity analysis.

The behavior of the growth rate as a function of substrate temperature for different  $\Phi_R$  can be divided in three regions as shown in Figure 3. At low substrate temperatures near 180 °C, where the re-evaporation rate of Te is too low, all extra Te atoms practically stick to the surface, leading to higher growth rates up to 0.9 Å/s. As the temperature rises to 220 °C in region A, the Te re-evaporation rate increases and the growth rate resembles the sticking coefficient curve of tellurium.<sup>28</sup> In the intermediate region B, for substrate temperatures between 220 °C and 280 °C, the exceeding Te atoms have sufficient energy to re-evaporate and the growth dynamics allows the Bi and Te atoms to accommodate in their sites. Therefore, the growth rate remains almost constant at around 0.2 Å/s and is only determined by the Bi<sub>2</sub>Te<sub>3</sub> cell temperature. For substrate temperatures higher than 280 °C (region C), the growth rates start to decrease and vanish at  $T_{\text{SUB}} > 300$  °C for  $\Phi_R = 0$  and at  $T_{\text{SUB}} > 310$  °C for  $\Phi_R = 1$ , due to the decrease of Bi sticking coefficient.<sup>28</sup> Contrary to region B, where the growth rate is independent of  $\Phi_R$ , the reduction of the growth rates in region C is more pronounced for lower  $\Phi_R$ .

### Reflection high energy electron diffraction

The reciprocal of the hexagonal surface lattice shown in Figure 2(b) is also a hexagonal lattice rotated by 30° with a lattice parameter of  $4\pi/a\sqrt{3}$ . In this sense, the symmetry azimuths during RHEED measurements are gyrated by 30° in relation to those shown in Figure 2(b). All RHEED patterns were measured with an energy of 16 keV.

In order to investigate the initial stages of the epitaxy of Bi<sub>2</sub>Te<sub>3</sub> on (111) BaF<sub>2</sub>, RHEED patterns were recorded during the first minutes of growth. Figure 4(a) shows the streaky RHEED pattern of the BaF<sub>2</sub> substrate along the  $[\bar{1}01]$

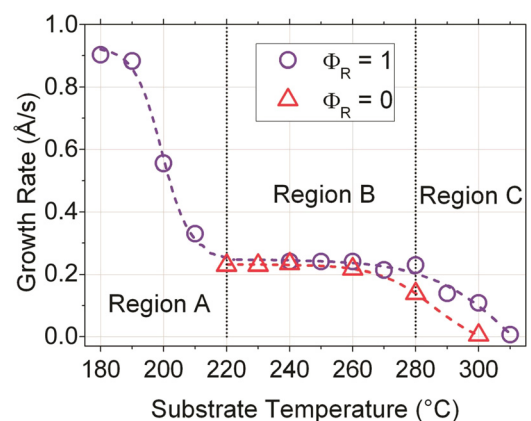


FIG. 3. Growth rate as a function of substrate temperature for flux ratio  $\Phi_R = 0$  and 1. In region A, the growth rate decreases from 0.9 to near 0.2 Å/s resembling the Te sticking coefficient temperature behavior. Between 220 and 280 °C, region B, a constant growth rate is achieved regardless of the extra Te flux. Above 280 °C in region C, the growth rates start to reduce due to the decreasing Bi sticking coefficient and vanish above a certain temperature depending on  $\Phi_R$ . All films were grown during 2 h.

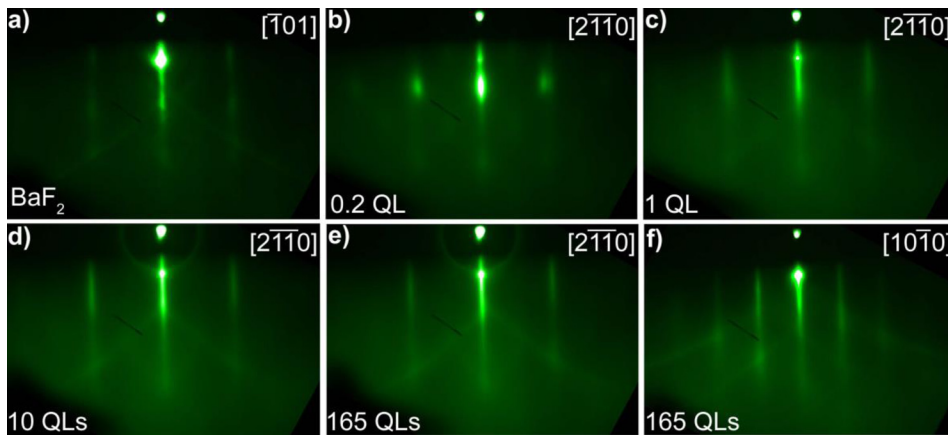


FIG. 4. RHEED patterns acquired during the epitaxy of  $\text{Bi}_2\text{Te}_3$  on (111)  $\text{BaF}_2$  substrate: (a)  $\text{BaF}_2$  surface just before growth and for increasing  $\text{Bi}_2\text{Te}_3$  film coverage after (b) 0.2 QL, (c) 1 QL, and (d) 10 QLs of deposition and at the end of growth with 165 QLs for both (e)  $[2\bar{1}\bar{1}0]$  and (f)  $[10\bar{1}0]$  azimuths.

azimuth just before growth, evidencing a flat surface. The RHEED patterns along the  $[2\bar{1}\bar{1}0]$  azimuth of the (0001)  $\text{Bi}_2\text{Te}_3$  film after 0.2 QL, 1 QL, and 10 QLs of deposition are shown in Figures 4(b)–4(d), respectively, for a sample grown at substrate temperature of  $240^\circ\text{C}$  and flux ratio  $\Phi_R = 1$ . The streaks of the  $\text{Bi}_2\text{Te}_3$  layer pattern start to be formed already with 0.2 QL of deposition. They become more elongated with 1 QL of coverage and, for a thickness of 10 QLs, the streaky RHEED pattern is completely formed with clearly defined Kikuchi lines. RHEED images with well defined streaks confirm the layer-by-layer growth mode since the early stages. The RHEED pattern measured along the  $[2\bar{1}\bar{1}0]$  azimuth for the film with 165 QLs at the end of growth, shown in Figure 4(e), is identical to the one measured with 10 QLs, indicating that the growing surface has the same characteristics throughout the whole deposition. The RHEED image measured along the  $[10\bar{1}0]$  azimuth, at the end of growth, for the same sample is shown in Figure 4(f) and also exhibits a streaky pattern with Kikuchi lines without intermediate streaks, confirming the absence of surface reconstruction for this epitaxy. Similar results were observed for all samples grown with substrate temperatures higher than  $220^\circ\text{C}$  and for all flux ratios.

The  $\text{Bi}_2\text{Te}_3$  films grown on region A exhibit a rough surface with Te agglomerates, as determined from energy dispersive x-ray field-emission gun microscopy analysis and broad x-ray diffraction peaks characteristic of films with poor crystalline quality and mixed phases. Therefore, the investigation in region A was not expanded to other flux ratios than  $\Phi_R = 1$ . The *ex situ* characterization results are presented in the next sessions for the films grown with  $T_{\text{SUB}} > 220^\circ\text{C}$  (regions B and C).

### X-ray diffraction

For all samples,  $\omega/2\Theta$  scans were recorded in a wide range of  $2\Theta$ , from  $4^\circ$  to  $104^\circ$ . Figure 5(a) shows the x-ray diffraction curves in terms of the reciprocal space coordinate along the  $[0001]$  direction ( $Q_z$ ) for films grown with fixed flux ratio  $\Phi_R = 1$  and varied substrate temperature from  $220^\circ\text{C}$  to  $300^\circ\text{C}$ , while Figure 5(b) displays them for a fixed  $T_{\text{SUB}} = 280^\circ\text{C}$  and  $\Phi_R$  ranging from 0 to 2. For all measured diffraction curves, besides the (111), (222), and (333)  $\text{BaF}_2$  substrate Bragg peaks, only the (000L)  $\text{Bi}_2\text{Te}_3$  symmetrical

diffraction peaks are observed, as expected for epitaxy occurring with the (000L)  $\text{Bi}_2\text{Te}_3$  hexagonal planes parallel to the (111)  $\text{BaF}_2$  surface.

For increasing substrate temperature at a fixed flux ratio, the (000L) x-ray diffraction peaks shift, become broader, or even split. This behavior is more pronounced for the  $\text{Bi}_2\text{Te}_3$  peaks with  $L = 18$  and  $L = 21$  and the expanded views of the diffraction curves around these maxima are shown in Figures 5(c) and 5(d), respectively. As  $T_{\text{SUB}}$  rises from  $220^\circ\text{C}$  to  $300^\circ\text{C}$  for  $\Phi_R = 1$ , the (00018)  $\text{Bi}_2\text{Te}_3$  peak slightly shifts to lower  $Q_z$  in direction to the peak position of the (00014) BiTe phase (red vertical line in Figure 5(c)), while the (00021)  $\text{Bi}_2\text{Te}_3$  Bragg peak moves to higher  $Q_z$  values towards the (00017) BiTe peak (red vertical line in Figure 5(d)), tending to Bi-rich phases. At lower substrate temperatures ( $T_{\text{SUB}} < 250^\circ\text{C}$ ), the x-ray diffraction curves do not present a significant change as a function of flux ratio. On the other hand, for higher substrate temperatures, the effect of the flux ratio variation on the x-ray curves is easily noticed. The influence of the extra Te flux is illustrated in Figures 5(e) and 5(f), where the expanded views in the vicinity of the  $L = 18$  and 21  $\text{Bi}_2\text{Te}_3$  peaks are represented. The large Te desorption at the elevated  $T_{\text{SUB}}$  of  $280^\circ\text{C}$  is compensated by increasing  $\Phi_R$  and plain  $\text{Bi}_2\text{Te}_3$  phase is recovered for  $\Phi_R = 2$ .

It is important to stress out that the  $\text{Bi}_x\text{Te}_y$  films grown in this work on (111)  $\text{BaF}_2$  substrates, using a nominal  $\text{Bi}_2\text{Te}_3$  solid source and extra Te cell, never presented pure BiTe phase even without offering additional Te flux ( $\Phi_R = 0$ ) and at the highest  $T_{\text{SUB}} = 300^\circ\text{C}$  (for  $T_{\text{SUB}} > 300^\circ\text{C}$ , no deposition is observed at all). These results are different from previously published,<sup>24,25</sup> where  $\text{Bi}_x\text{Te}_y$  epitaxial film with composition ranging from BiTe to  $\text{Bi}_2\text{Te}_3$  was obtained by varying only the exceeding Te flux. This fact can be explained by a variation in the stoichiometry of the  $\text{Bi}_2\text{Te}_3$  solid sources used in the different MBE machines.

To investigate the effect of the Te deficit in the  $Q_z$  scans, reflection and transmission coefficients of stacking sequences of QLs and BLs were calculated by using a set of recursive equations<sup>29</sup> that accounts for absorption, refraction, and rescattering events in the film, as well as in the substrate lattice. Figure 6 shows the calculated diffraction curves for an ordered  $\text{Bi}_2\text{Te}_3$  film with 165 QLs and for an ordered  $\text{Bi}_4\text{Te}_5$  film with 33  $\text{Bi}_2$  BLs inserted in between 165 QLs. The

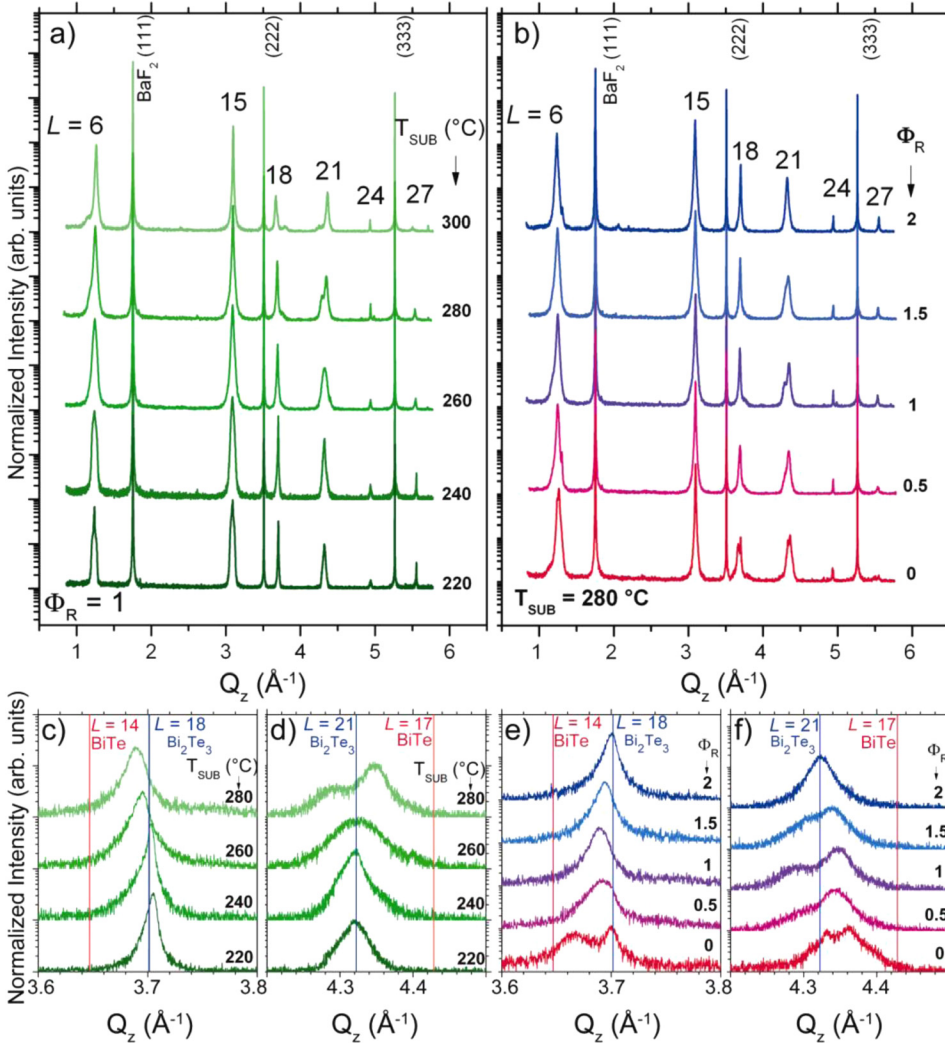


FIG. 5. Wide angular  $\omega/2\theta$  scans of  $\text{Bi}_2\text{Te}_3$  epitaxial films grown on (111)  $\text{BaF}_2$  at (a) different substrate temperatures  $T_{\text{SUB}}$  and fixed flux ratio  $\Phi_R = 1$  and (b) at varied flux ratio  $\Phi_R$  from 0 to 2 and fixed  $T_{\text{SUB}} = 280^\circ\text{C}$ . (c)–(f) Expanded view of the scans around the  $L = 18$  and  $L = 21$   $\text{Bi}_2\text{Te}_3$  peaks. Blue and red vertical reference lines indicate the expected peak positions for epitaxial films of  $\text{Bi}_2\text{Te}_3$  and  $\text{BiTe}$ , respectively.

diffraction pattern of the ordered  $\text{Bi}_4\text{Te}_5$  film is quite different from that of the  $\text{Bi}_2\text{Te}_3$ , indicating that all films have structures close to  $\text{Bi}_2\text{Te}_{3-\delta}$  with  $\delta < 0.5$ . The peak near  $Q_z = 3.1 \text{ \AA}^{-1}$  ( $L = 15$  in the  $\text{Bi}_2\text{Te}_3$  structure) shifts according to  $Q_z = 2\pi/\langle\Delta z\rangle$ , where the mean inter-plane atomic distance  $\langle\Delta z\rangle$  is given by

$$\langle\Delta z\rangle = 2.035 - 0.025 \delta (\text{\AA}) \quad (1)$$

and accounts for contributions of both composition and strain variations for epitaxial films on (111)  $\text{BaF}_2$ .<sup>25</sup> It implies that the  $\text{Bi}_2\text{Te}_3$  (M:N=0:3),  $\text{Bi}_4\text{Te}_5$  (M:N=1:5), and  $\text{BiTe}$  (M:N=1:2) films have lattice periodicities of  $30.525 \text{ \AA}$  ( $=15 \langle\Delta z\rangle$ ),  $54.608 \text{ \AA}$  ( $=27 \langle\Delta z\rangle$ ), and  $24.120 \text{ \AA}$  ( $=12 \langle\Delta z\rangle$ ), respectively. The other effect that can be verified by the simulation as a consequence of small Te deficit ( $\delta < 0.5$ ) is the splitting of the  $L = 21$  peak into two peaks of nearly the same intensity, which is roughly given by

$$\Delta Q_z \approx 0.23\delta (\text{\AA}^{-1}). \quad (2)$$

The  $L = 18$  also splits by the same amount, but one of the peaks is weaker than the other with the stronger peak shifting to the left.

Figure 7(a) shows the  $\langle\Delta z\rangle$  values obtained from the  $L = 15$  peak position as a function of the substrate temperature for  $\Phi_R = 0, 1$ , and 2. By comparing with the expected  $\langle\Delta z\rangle$  values for epitaxial films of phases from  $\text{Bi}_2\text{Te}_3$  to  $\text{BiTe}$  (reference lines in Figure 7(a)), it is easy to notice that the films start to deviate from  $\text{Bi}_2\text{Te}_3$  to Bi-rich phases for substrate temperatures higher than  $250^\circ\text{C}$  when  $\Phi_R = 0$  and 1. For higher additional Te flux ( $\Phi_R = 2$ ), the measured  $\langle\Delta z\rangle$  values indicate that stoichiometric  $\text{Bi}_2\text{Te}_3$  epitaxial films are

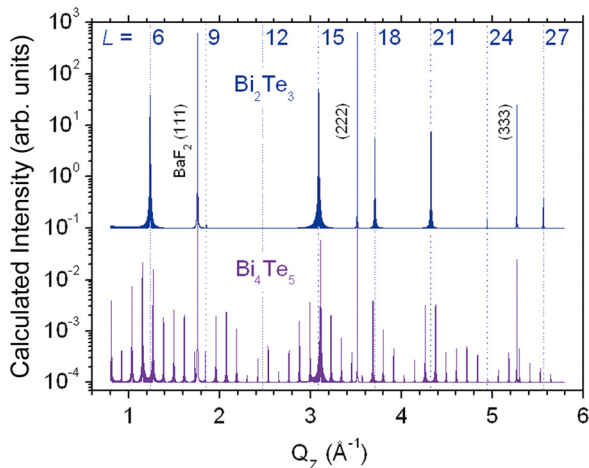


FIG. 6. Calculated x-ray diffraction curves for ordered  $\text{Bi}_2\text{Te}_3$  (with 165 QLs) and  $\text{Bi}_4\text{Te}_5$  (with 33 BLs periodically inserted in 165 QLs) films on (111)  $\text{BaF}_2$  substrate.

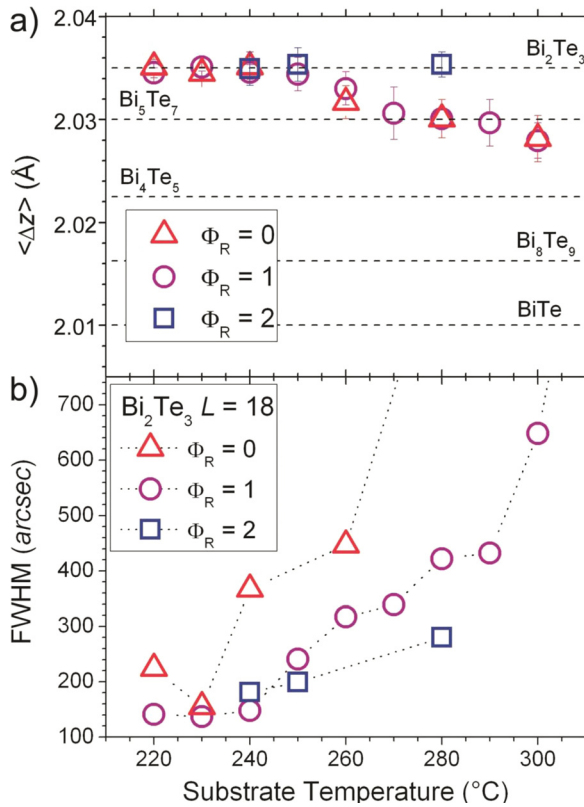


FIG. 7. (a) Mean inter-plane atomic distance  $\langle \Delta z \rangle$  as a function of substrate temperature. Reference values (dashed lines) of a few phases are also shown for sake of comparison. (b) Full-width at half maximum (FWHM) of the (00018) Bi<sub>2</sub>Te<sub>3</sub> Bragg peak for different flux ratios  $\Phi_R$ .

achieved up to  $T_{\text{SUB}}$  of 280 °C. According to this, the composition of the Bi<sub>x</sub>Te<sub>y</sub> epitaxial films reported in this work stays between Bi<sub>2</sub>Te<sub>3</sub> and Bi<sub>4</sub>Te<sub>5</sub>, i.e., with the Te deficit  $\delta < 0.5$ . Shifting and splitting of the  $L = 18$  and  $L = 21$  peaks are also observed in the films with higher  $\delta$  values. For instance, the film grown at  $T_{\text{SUB}}$  of 280 °C and  $\Phi_R = 1$ , the splitting of the  $L = 21$  peak is about  $\Delta Q_z = 0.056 \text{ \AA}^{-1}$  (Figure 5(d)), providing an estimated Te deficit  $\delta = 0.24$  (Eq. (2)), which agrees very well with  $\delta = 0.20$  (Eq. (1)) obtained from  $\langle \Delta z \rangle = 2.030 \text{ \AA}$  (Figure 7(a)).

The crystalline quality of the grown films can be evaluated by the width of the (00018) Bi<sub>2</sub>Te<sub>3</sub> x-ray diffraction peak. The  $\omega$ -scan around the (00018) peak was measured for all samples and its full-width at half-maximum (FWHM) is displayed in Figure 7(b) as function of substrate temperature and flux ratio. For  $\Phi_R = 1$ , the FWHM increases monotonically from 150 arcsec to 600 arcsec as  $T_{\text{SUB}}$  rises from 220 °C to 300 °C, while without extra Te flux, the crystalline quality gets worse as it increases from 200 arcsec to values higher than 1000 arcsec in the same temperature range. As the flux ratio increases to  $\Phi_R = 2$ , the FWHM remains below 300 arcsec up to  $T_{\text{SUB}} = 280 \text{ °C}$ .

### Twinning characterization

To investigate the epitaxial relations of the Bi<sub>2</sub>Te<sub>3</sub> films on (111) BaF<sub>2</sub> substrates, azimuthal scans from 0° to 360° were measured for the fixed (01 $\bar{1}$ 5) asymmetric x-ray diffraction peak.

Figure 8 shows the azimuthal scans for films grown at two substrate temperatures. The major peaks at  $\phi = 0^\circ$ ,  $120^\circ$ , and  $240^\circ$ , labeled as A, correspond to the three-fold symmetry of the Bi<sub>2</sub>Te<sub>3</sub> structure shown in Figure 2(b), evidencing that the  $[11\bar{2}0]$  azimuth of the film hexagonal lattice is parallel to the  $[\bar{1}10]$  azimuth of the substrate cubic lattice. The azimuthal scans also show additional peaks at  $\phi = 60^\circ$ ,  $180^\circ$ , and  $300^\circ$ , labeled as B, corresponding to twinned domains rotated by  $180^\circ$ . The twinning degree can be expressed by the mean intensity ratio between both peaks,  $\text{TwD} = \langle I_B \rangle / \langle I_A \rangle$ . Values of TwD close to zero indicate small portion of twinned domains, while TwD values close to one mean that the quantity of twinned domains is practically equal to the untwinned regions. Here, all twinning analyses were made on pure Bi<sub>2</sub>Te<sub>3</sub> epitaxial films ( $\langle \Delta z \rangle = 2.035 \pm 0.002 \text{ \AA}$ ). Figure 9(a) plots TwD as a function of substrate temperature for different values of  $\Phi_R = 0, 1$ , and 2. One can observe that the twinning degree increases for increasing growth temperature and is lower for higher extra Te offer. The lowest TwD values near 0.01 were obtained at a growth temperature of 220 °C and flux ratio  $\Phi_R = 1$ . Twinning domains of hexagonal crystals with ABCABC stacking, like Bi<sub>2</sub>Te<sub>3</sub>, are formed by a change in the stacking sequence in different regions of the sample during epitaxial growth. Usually, higher energies are needed to generate twinning domains, since this stacking fault is energetically less favorable. Therefore, lower growth temperatures favor single domain films, as observed here. At a fixed substrate temperature (constant kinetic energy), the

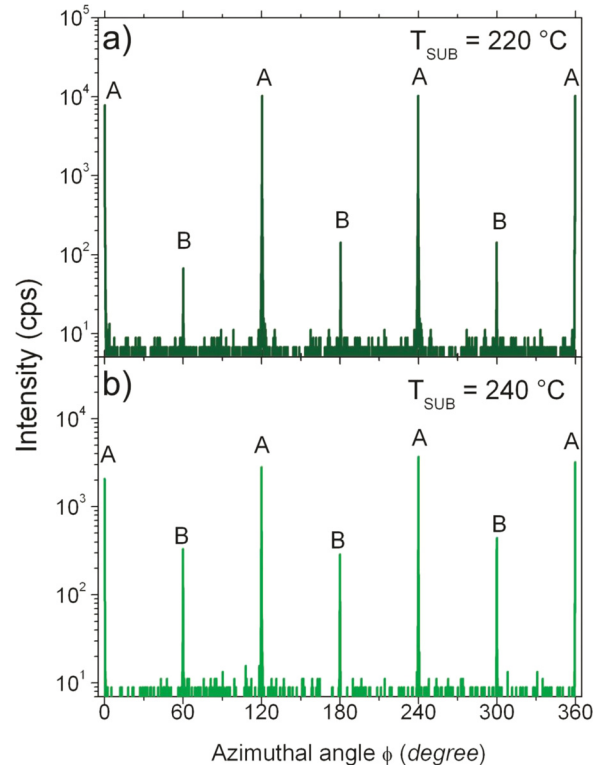


FIG. 8. Azimuthal scans for a fixed (01 $\bar{1}$ 5) asymmetric x-ray diffraction peak for Bi<sub>2</sub>Te<sub>3</sub> films grown at two different substrate temperatures and fixed flux ratio of 1. The major peaks labeled A correspond to the three-fold symmetry of Bi<sub>2</sub>Te<sub>3</sub> hexagonal lattice, with its  $[11\bar{2}0]$  azimuth parallel to the  $[\bar{1}10]$  direction of the BaF<sub>2</sub> substrate. The peaks labeled B are relative to twinned domains rotated by  $180^\circ$ .

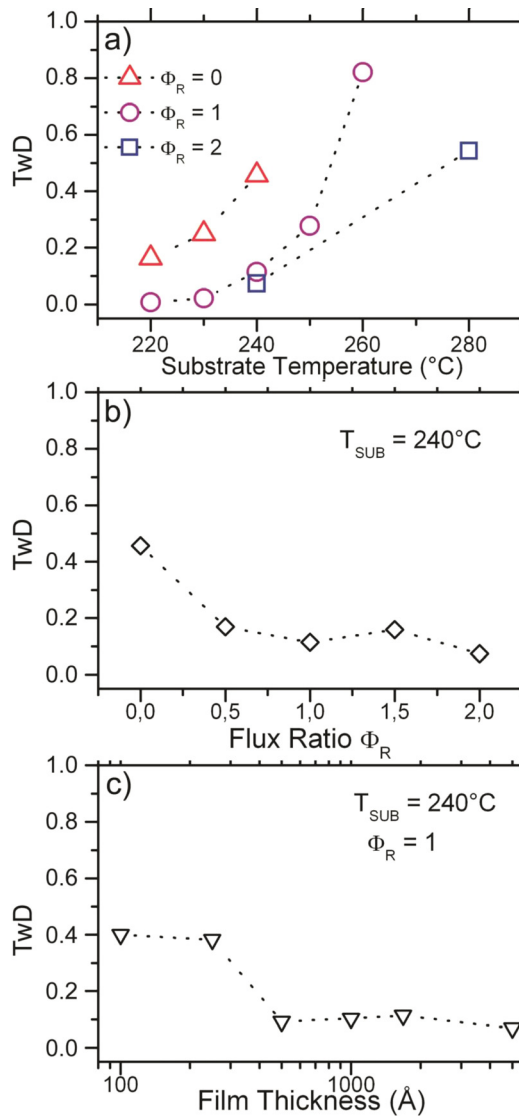


FIG. 9. Twinning degree (TwD) of the Bi<sub>2</sub>Te<sub>3</sub> films as a function of (a) substrate temperature for different flux ratios  $\Phi_R = 0, 1, \text{ and } 2$ , (b) flux ratio  $\Phi_R$  at a fixed  $T_{\text{SUB}} = 240^\circ\text{C}$ , and (c) film thickness.

offer of extra Te atoms increases the probability of formation of Bi-Te bonds, which reduces the system energy and promotes primary domains. Figure 9(b) shows the dependence of TwD on flux ratio  $\Phi_R$  for a fixed substrate temperature ( $240^\circ\text{C}$ ), confirming that the exceeding Te flux favors single domain films. The behavior of TwD on film thickness is shown in Figure 9(c) for Bi<sub>2</sub>Te<sub>3</sub> layers grown at  $T_{\text{SUB}} = 240^\circ\text{C}$  and  $\Phi_R = 1$ . It remains near 0.4 for thickness between  $100 \text{ \AA}$  and  $250 \text{ \AA}$ , drops to a value of 0.1 for a thickness of  $500 \text{ \AA}$ , and maintains nearly constant at this value up to  $5000 \text{ \AA}$ , indicating that the twinning occurs since the initial stages of growth.

### X-ray reflectometry

The x-ray reflectivity curves were measured with a  $\omega/2\Theta$  scan from  $\omega = 0.05^\circ$  to  $2.0^\circ$  for all samples. The open circles in the graph of Figure 10(a) represent typical curves for samples grown in region B of Figure 3. This curve

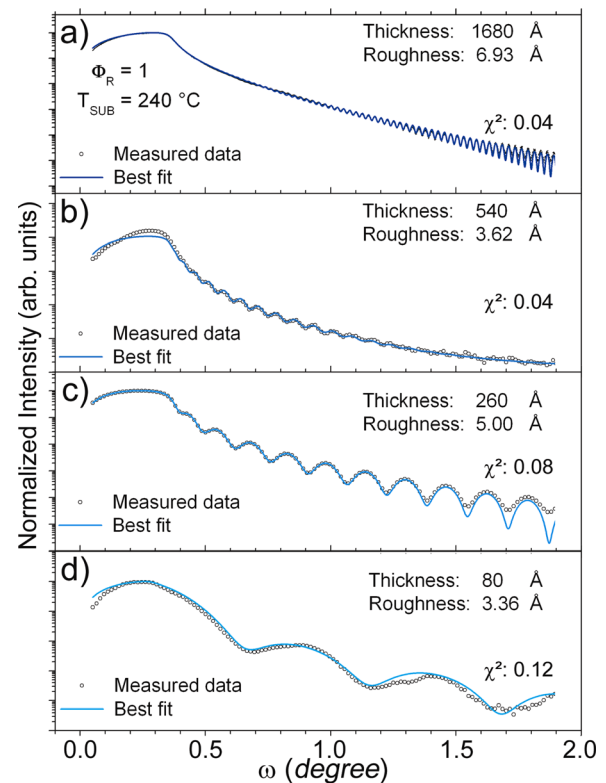


FIG. 10. Measured x-ray reflectivity curves (open circles) of Bi<sub>2</sub>Te<sub>3</sub>/BaF<sub>2</sub> films grown at fixed substrate temperature  $T_{\text{SUB}} = 240^\circ\text{C}$  and flux ratio  $\Phi_R = 1$  with decreasing deposition time: (a) 120, (b) 36, (c) 18, and (d) 7 min, leading to a series with varied thickness. The solid lines are calculated curves that best fitted to the measured data. The values of layer thickness and roughness extracted from the best fits are displayed in the graphs.

exhibits very well defined interference fringes, which indicates a homogeneous layer with a smooth surface and allows an accurate determination of the film thickness. Due to the rougher surface of the films grown in region A and to the thickness inhomogeneity of the ones grown in region C, the reflectivity curves of these films present attenuated or even no interference fringes.

Besides the films deposited during 2 h, a set of Bi<sub>2</sub>Te<sub>3</sub>/BaF<sub>2</sub> films with varied thickness was produced for the reflectometry analysis. The growth parameters at fixed  $T_{\text{SUB}} = 240^\circ\text{C}$  and  $\Phi_R = 1$  inside region B were chosen to ensure that pure high-quality Bi<sub>2</sub>Te<sub>3</sub> films are obtained for this series. The samples were grown with varied deposition time of 36, 18, and 7 min and their measured reflectivity curves are shown with open circles in Figures 10(b), 10(c), and 10(d), respectively.

In order to extract quantitative information from the reflectometry measurements, x-ray reflectivity curves were calculated using the GenX software<sup>30</sup> and fitted to the measured ones. The main fitting parameters are the layer thickness and roughness. The real ( $\gamma$ ) and imaginary ( $\beta$ ) parts of the material refractive index ( $n = 1 - \gamma - i\beta$ ) obtained from the GenX database are also parameters in the simulation. For the BaF<sub>2</sub> substrate, the tabulated values ( $\gamma = 1.306 \times 10^{-5}$  and  $\beta = 0.153 \times 10^{-5}$ ) were used and kept fixed. These parameters were left free for the Bi<sub>2</sub>Te<sub>3</sub> layer during the simulation and their values, after reaching the best fit, remained

within +4.7% relative to the tabulated  $\text{Bi}_2\text{Te}_3$  values ( $\gamma = 1.972 \times 10^{-5}$  and  $\beta = 0.232 \times 10^{-5}$ ). In the GenX simulation, the roughness is assumed to have a Gaussian distribution and is included as corrective factors to electric field amplitudes at the interfaces according to the Nevot–Croce model. The substrate roughness was left as a free parameter during the simulation process and its value after the best fit remained near 3 Å for all samples. The goodness of the fit is evaluated through the mean square deviation between the calculated and measured logarithmic intensities ( $\chi^2$ ). The best fit for each sample is also plotted as solid line in the graphs of Figure 10 and the values of the layer thickness and roughness that came out from the best fits are displayed in the graphs. The excellent agreement between the measured and simulated curves, evidenced by the small values of  $\chi^2$ , demonstrates that homogeneous and smooth  $\text{Bi}_2\text{Te}_3$  epitaxial layers can be obtained at optimized growth conditions even for a thin film of only 8 QLs.

## CONCLUSION

A systematic investigation of the bismuth telluride epitaxial growth on (111)  $\text{BaF}_2$  as a function of substrate temperature and  $\text{Te}/\text{Bi}_2\text{Te}_3$  beam flux ratio was presented. RHEED analysis revealed that a layer-by-layer growth mode is observed since the early stages of epitaxy and remains throughout the whole deposition. Three regimes were determined for the growth rate dependence on substrate temperature: (i) a low temperature region, where the growth rate decreases resembling the Te sticking coefficient curve; (ii) an intermediate region, in which the growth rate remains constant independent of the additional Te flux; and (iii) a third region at higher temperatures, where it diminishes again until vanishing, due to the reduction of Bi sticking coefficient. The intermediate region is found to be the most suitable to grow high quality  $\text{Bi}_2\text{Te}_3$  thin films.

X-ray diffraction analysis showed that the epitaxy occurs with the (000 $L$ )  $\text{Bi}_2\text{Te}_3$  hexagonal planes parallel to the (111)  $\text{BaF}_2$  surface. Comparison of the measured diffraction curves with calculations established that the composition of the  $\text{Bi}_x\text{Te}_y$  epitaxial films produced in this work stays between  $\text{Bi}_2\text{Te}_3$  and  $\text{Bi}_4\text{Te}_5$ , with a Te deficit from 0 to 0.3. Films with pure BiTe phase were never obtained even at the highest substrate temperature and with no additional Te flux. Line width of the  $L = 18$  diffraction peak as low as 140 arcsec was measured for the  $\text{Bi}_2\text{Te}_3$  thin films, which demonstrates the high crystalline quality obtained. Azimuthal scans for a fixed asymmetrical diffraction peak showed that twinned domains rotated by 180° are present in the films. Twinning degree rises with increasing substrate temperature and this dependence is less pronounced for higher flux ratios. It is also found to reduce as the film thickness increases.

For the pure  $\text{Bi}_2\text{Te}_3$  films grown in the optimized conditions, the x-ray reflectivity curves exhibited well defined interference fringes, characteristic of homogeneous layers with smooth surface. Layer thickness and roughness were accurately determined by fitting the experimental data to the calculated curves.

The results presented in this work demonstrate that  $\text{Bi}_2\text{Te}_3$  films with very well controlled structural parameters can be obtained in a reproducible manner. The high structural quality of  $\text{Bi}_2\text{Te}_3$  films as thin as only 8 QLs grown here indicates that they are promising candidates for intrinsic topological insulator, in which the bulk conduction is suppressed and only the metallic surface states are present.

## ACKNOWLEDGMENTS

The authors acknowledge CNPq (Grant Nos. 142191/2014-0, 302134/2014-0, 307933/2013-0, and 306982/2012-9) and FAPESP (Grant No. 2014/04150-0) for financial support.

- <sup>1</sup>D. A. Wright, "Thermoelectric properties of bismuth telluride and its alloys," *Nature* **181**, 834–834 (1958).
- <sup>2</sup>L. D. Hicks and M. S. Dresselhaus, "Effect of quantum-well structures on the thermoelectric figure of merit," *Phys. Rev. B* **47**, 12727–12731 (1993).
- <sup>3</sup>R. Venkatasubramanian, E. Siivola, T. Colpitts, and B. O'Quinn, "Thin-film thermoelectric devices with high room-temperature figures of merit," *Nature* **413**, 597–602 (2001).
- <sup>4</sup>J. E. Moore, "The birth of topological insulators," *Nature* **464**, 194–198 (2010).
- <sup>5</sup>M. Z. Hasan and C. L. Kane, "Colloquium: Topological insulators," *Rev. Mod. Phys.* **82**, 3045–3067 (2010).
- <sup>6</sup>Y. Ando, "Topological insulator materials," *J. Phys. Soc. Jpn.* **82**, 102001 (2013).
- <sup>7</sup>L. Fu, C. L. Kane, and E. J. Mele, "Topological insulators in three dimensions," *Phys. Rev. Lett.* **98**, 106803 (2007).
- <sup>8</sup>L. Fu and C. L. Kane, "Topological insulators with inversion symmetry," *Phys. Rev. B* **76**, 045302 (2007).
- <sup>9</sup>H. Zhang, C.-X. Liu, X.-L. Qi, X. Dai, Z. Fang, and S.-C. Zhang, "Topological insulators in  $\text{Bi}_2\text{Se}_3$ ,  $\text{Bi}_2\text{Te}_3$  and  $\text{Sb}_2\text{Te}_3$  with a single Dirac cone on the surface," *Nat. Phys.* **5**, 438–442 (2009).
- <sup>10</sup>D. Hsieh, D. Qian, L. Wray, Y. Xia, Y. S. Hor, R. J. Cava *et al.*, "A topological Dirac insulator in a quantum spin Hall phase," *Nature* **452**, 970–974 (2008).
- <sup>11</sup>D. Hsieh, Y. Xia, D. Qian, L. Wray, J. H. Dil, F. Meier *et al.*, "A tunable topological insulator in the spin helical Dirac transport regime," *Nature* **460**, 1101–1105 (2009).
- <sup>12</sup>Y. Xia, D. Qian, D. Hsieh, L. Wray, A. Pal, H. Lin *et al.*, "Observation of a large-gap topological-insulator class with a single Dirac cone on the surface," *Nat. Phys.* **5**, 398–402 (2009).
- <sup>13</sup>D. Hsieh, Y. Xia, D. Qian, L. Wray, F. Meier, J. Dil *et al.*, "Observation of time-reversal-protected single-Dirac-cone topological-insulator states in  $\text{Bi}_2\text{Te}_3$  and  $\text{Sb}_2\text{Te}_3$ ," *Phys. Rev. Lett.* **103**, 146401 (2009).
- <sup>14</sup>Y. L. Chen, J. G. Analytis, J.-H. Chu, Z. K. Liu, S.-K. Mo, X. L. Qi *et al.*, "Experimental realization of a three-dimensional topological insulator,  $\text{Bi}_2\text{Te}_3$ ," *Science* **325**, 178–181 (2009).
- <sup>15</sup>S. R. Park, W. S. Jung, C. Kim, D. J. Song, C. Kim, S. Kimura *et al.*, "Quasiparticle scattering and the protected nature of the topological states in a parent topological insulator  $\text{Bi}_2\text{Se}_3$ ," *Phys. Rev. B* **81**, 041405 (2010).
- <sup>16</sup>L. V. Yashina, J. Sánchez-barriga, M. R. Scholz, A. a. Volykhov, A. P. Sirotnina, V. S. Neudachina *et al.*, "Negligible surface reactivity of topological insulators  $\text{Bi}_2\text{Se}_3$  and  $\text{Bi}_2\text{Te}_3$  towards oxygen and water," *ACS Nano* **7**, 5181–5191 (2013).
- <sup>17</sup>H. Bando, K. Koizumi, Y. Oikawa, K. Daikohara, V. A. Kulbachinskii, and H. Ozaki, "The time-dependent process of oxidation of the surface of  $\text{Bi}_2\text{Te}_3$  studied by x-ray photoelectron spectroscopy," *J. Phys.: Condens. Matter* **12**, 5607–5616 (2000).
- <sup>18</sup>G. Wang, X.-G. Zhu, Y.-Y. Sun, Y.-Y. Li, T. Zhang, J. Wen *et al.*, "Topological insulator thin films of  $\text{Bi}_2\text{Te}_3$  with controlled electronic structure," *Adv. Mater.* **23**, 2929–2932 (2011).
- <sup>19</sup>J. Park, Y.-A. Soh, G. Aeppli, S. R. Bland, X.-G. Zhu, X. Chen *et al.*, "Crystal structure and epitaxy of  $\text{Bi}_2\text{Te}_3$  films grown on Si," *Appl. Phys. Lett.* **101**, 221910 (2012).

- <sup>20</sup>A. Fülöp, Y. Song, S. Charpentier, P. Shi, M. Ekström, L. Galletti *et al.*, “Phase transition of bismuth telluride thin films grown by MBE,” *Appl. Phys. Express* **7**, 045503 (2014).
- <sup>21</sup>X. Liu, D. J. Smith, J. Fan, Y.-H. Zhang, H. Cao, Y. P. Chen *et al.*, “Structural properties of Bi<sub>2</sub>Te<sub>3</sub> and Bi<sub>2</sub>Se<sub>3</sub> topological insulators grown by molecular beam epitaxy on GaAs(001) substrates,” *Appl. Phys. Lett.* **99**, 171903 (2011).
- <sup>22</sup>L. He, X. Kou, and K. L. Wang, “Review of 3D topological insulator thin-film growth by molecular beam epitaxy and potential applications,” *Phys. Status Solidi RRL* **7**, 50–63 (2013).
- <sup>23</sup>N. Peranio, O. Eibl, and J. Nurnus, “Structural and thermoelectric properties of epitaxially grown Bi<sub>2</sub>Te<sub>3</sub> thin films and superlattices,” *J. Appl. Phys.* **100**, 114306 (2006).
- <sup>24</sup>O. Caha, A. Dubroka, V. Holy, H. Steiner, O. Rader, T. N. Stanislavchuk *et al.*, “Growth, structure and electronic properties of epitaxial bismuth telluride topological insulator films on BaF<sub>2</sub> (111) substrates,” *Cryst. Growth Des.* **13**, 3365–3373 (2013).
- <sup>25</sup>H. Steiner, V. Volobuev, O. Caha, G. Bauer, G. Springholz, and V. Holý, “Structure and composition of bismuth telluride topological insulators grown by molecular beam epitaxy,” *J. Appl. Crystallogr.* **47**, 1889–1900 (2014).
- <sup>26</sup>K. Hofer, C. Becker, D. Rata, J. Swanson, P. Thalmeier, and L. H. Tjeng, “Intrinsic conduction through topological surface states of insulating Bi<sub>2</sub>Te<sub>3</sub> epitaxial thin films,” *Proc. Natl. Acad. Sci. U.S.A.* **111**, 14979–14984 (2014).
- <sup>27</sup>J. W. G. Bos, H. W. Zandbergen, M.-H. Lee, N. P. Ong, and R. J. Cava, “Structures and thermoelectric properties of the infinitely adaptive series (Bi<sub>2</sub>)<sub>m</sub>(Bi<sub>2</sub>Te<sub>3</sub>)<sub>n</sub>,” *Phys. Rev. B* **75**, 195203 (2007).
- <sup>28</sup>A. Mzard, D. Sayah, G. Brun, J. C. Tedenac, and A. Boyer, “Crystal growth and sticking coefficient of Bi<sub>2</sub>Te<sub>3</sub> thin films on Si(111) substrate,” *J. Mater. Sci. Lett.* **14**, 194–197 (1995).
- <sup>29</sup>S. L. Morelhão, *Computer Simulation Tools for X-ray Analysis* (Springer International Publishing, Cham, 2016).
- <sup>30</sup>M. Björck and G. Andersson, “GenX: An extensible X-ray reflectivity refinement program utilizing differential evolution,” *J. Appl. Crystallogr.* **40**, 1174–1178 (2007).